Applied Catalysis B: Environmental 176–177 (2015) 240–248

Contents lists available at ScienceDirect

Applied Catalysis B: Environmental

journal homepage: www.elsevier.com/locate/apcatb

A simple strategy for fabrication of Pd@MIL-100(Fe) nanocomposite as a visible-light-driven photocatalyst for the treatment of pharmaceuticals and personal care products (PPCPs)

Ruowen Liang, Shuiguang Luo, Fenfen Jing, Lijuan Shen, Na Qin, Ling Wu *

State Key Laboratory of Photocatalysis on Energy and Environment, Fuzhou University, Fuzhou 350002, PR China

ARTICLE INFO

Article history:
Received 4 February 2015
Received in revised form 31 March 2015
Accepted 5 April 2015
Available online 7 April 2015

Keywords:
MIL-100(Fe)
Pd nanoparticles
Photocatalysis
PPCPs
Visible-light

ABSTRACT

The effective treatment of pharmaceutical and personal care products (PPCPs) contained wastewater remains a significant but challenging task for the environmental restoration. In this work, a novel Pd@MIL-100(Fe) nanocomposite has been successfully fabricated *via* a facile alcohol reduction approach. The resulting Pd@MIL-100(Fe) has exhibited superior photoactivity toward degradation of three typical PPCPs, that is theophylline, ibuprofen and bisphenol A, under visible light irradiation ($\lambda \geq 420$ nm). Its photoactivity is also much higher than that of original-MIL-100(Fe). Combining with photoelectrochemical analyses, it could be revealed that the introduction of Pd NPs would minimize the recombination of photogenerated electron–hole pairs, thereby improving the photocatalytic performance. Furthermore, the effects of different kinds of metals, the loading amount of noble-metal, the pH value of reaction solution and initial concentration of hydrogen peroxide on the photocatalytic degradation activities have been measured in detail. In addition, a possible photocatalytic reaction mechanism has been investigated. This work has not only represented the first example of using the MOFs photocatalysts to remove the aqueous PPCPs, but also offered useful information on the fabrication of efficient MOF photocatalysts for environmental restoration.

1. Introduction

Pharmaceuticals and personal care products (PPCPs) are a type of chemical contaminants which include medications, ingredients in cosmetics, food supplements and dental care products [1]. Over the past decade, overwhelming evidences have shown that PPCPs are ubiquitous in surface water, ground water, and even some drinking water [2]. Due to their widespread use, incomplete removal during wastewater treatment, and the fact that their potential impact on the human health, PPCPs have been classified as pollutants of emerging concern [1–3]. Currently, various approaches have been employed to remove PPCPs from wastewater, such as biodegradation, biofiltration, ozonation and photocatalysis [4–9]. Among these approaches, photocatalysis is a promising technique since it achieves the one-pot removal of PPCPs by utilizing sunlight [10–12]. Until now, TiO_2 has been emerged as the most common photocatalyst for the treatment of PPCPs contained wastewater under UV irradiation [8,9]. However, because of low surface area and the lack of visible light response, TiO_2 would show restricted efficiency under solar illumination. Thus, it is highly desirable to design and seek efficient photocatalysts for the treatment of PPCPs under visible light.

Metal-organic frameworks (MOFs) are a new class of organic–inorganic hybrid solids, which became one of the fastest developing fields of chemistry [13]. Their unique properties such as structural flexibility and large specific surface area have led to the successful application of MOFs in magnetism, adsorption, sensor devices, drug release, and catalysis [14–20]. As the historic work made by García et al. in 2006, more and more attention has been paid to exploring the MOF materials as a new type of photocatalysts [21–24]. To further improve the photocatalytic performances of MOFs, some researchers focus their efforts on the introduction of functional entities into such materials [25,26]. Especially, great efforts have been paid to construct the metal@MOFs nanocomposites [27]. The methods currently adopted to support metal NPs on the MOF materials including impregnation, chemical vapor deposition or incipient wetness impregnation method. However, these synthetic strategies often suffered from the drawbacks of high energy consumption, requiring complicated multi-step synthesis and using strong reducing

* Corresponding author. Tel.: +86 591 83779362; fax: +86 591 83779105.
E-mail address: wuling@fzu.edu.cn (L. Wu).

http://dx.doi.org/10.1016/j.apcatb.2015.04.009
0926-3373/

agent such as $NaBH_4$, which may destroy the substrates [28,29]. Thus, it is of significance to implement a facile and simple approach for fabricating metal@MOF photocatalysts with novel structures and fascinating properties. Although there have been some reports on metal@MOF. It should be noted that they always focus on the study of catalytic activity or hydrogen storage [30,31], the reports on metal@MOF for photocatalytic applications are rather scarce. Especially, the utilization of MOFs in photocatalytic treatment of PPCPs under visible light has remained unavailable so far.

As a typical MOF material, MIL-100(Fe) is of special interest due to its high chemical stability and water stability, which makes it to be a judicious choice to couple with metal NPs. Besides, considering its photoactive property, MIL-100(Fe) in particular is a promising candidate for the development of efficient photocatalysts [32]. Toward this end, we herein report the synthesis of highly dispersed Pd NPs anchored on MIL-100(Fe) by a facile alcohol reduction approach using H_2PdCl_4 as palladium precursor. The photocatalytic performance of the Pd@MIL-100(Fe) nanocomposite has been evaluated by the degradation of three typical PPCPs, that is theophylline, ibuprofen and bisphenol A, under visible light irradiation ($\lambda \geq 420$ nm). The results have revealed that the as-synthesized Pd@MIL-100(Fe) exhibits high photoactivity toward degradation of PPCPs, which is also better than that of the blank MIL-100(Fe). Moreover, the visible light photocatalytic activity of Pd@MIL-100(Fe) is found to be closely dependent on the deposition of different noble-metals and the loading amount of Pd. In addiction, the various operational factors that affect PPCPs removal, including the pH value of the reaction solution and the initial concentration of hydrogen peroxide have also been investigated in detail. Finally, a possible photocatalytic reaction mechanism has been proposed.

2. Experimental

2.1. Reagents and chemicals

All reagents were used without further purification. Hydrogen tetrachloroaurate (III) tetrahydrate ($HAuCl_4{\cdot}4H_2O$), hexachloroplatinic (IV) acid hexahydrate ($H_2PtCl_6{\cdot}6H_2O$), palladium chloride ($PdCl_2$), hydrochloric acid (HCl, 37%), hydrofluoric acid (HF, 49%), nitric acid (HNO_3, 68%) and hydrogen peroxide (H_2O_2, 30%) were purchased from Sinopharm Chemical Reagent Co., Ltd. Fe powder (99%), polyvinylpyrrolidone (PVP, average Mw = 40,000) were supplied by Aladdin Reagent Co., Ltd. Benzene-1,3,5-tricarboxylic acid (H_3BTC, 99%) was supplied by Alfa Aesar China Co., Ltd.

2.2. Synthesis of MIL-100(Fe)

MIL-100(Fe) was prepared according to the previous reported [33]. Typically, a mixture of Fe powder, H_3BTC, HF, HNO_3 and H_2O with a molar ratio of 1:0.67:2:0.6:277 was transferred into a Teflon liner. After stirred at 500 rpm for 30 min, the Teflon liner was sealed in a stainless steel bomb and heated at 150 °C for 24 h. Saffron yellow MIL-100(Fe) powder was collected. A treatment in hot water (60 °C) for 3 h was applied to remove the residual H_3BTC. Then, the obtained saffron yellow powder was centrifuged at 4000 rpm for 5 min and dried under vacuum at 100 °C for 12 h.

2.3. Fabrication of Pd@MIL-100(Fe)

A schematic diagram of the synthesis procedure is shown in Scheme 1. H_2PdCl_4 aqueous solution (10 mg/mL) was prepared by dissolving $PdCl_2$ in HCl aqueous solution. In a typical experiment, a mixture of MIL-100(Fe) (100 mg), a certain amount of H_2PdCl_4 solution, PVP (0.0333 g), ethanol (3 mL) and H_2O (12 mL) was added into a 50 mL round bottom flask. After stirred for about 15 min, the resulting suspension was refluxed at 90 °C for 3 h. And then, the as-obtained brown Pd@MIL-100(Fe) powder was washed with ethanol for several times and blow-dried with N_2.

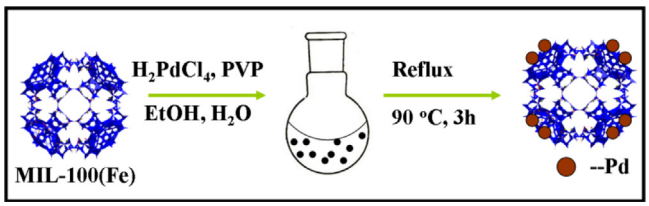

Scheme 1. Overall flowchart for fabrication of the Pd@MIL-100(Fe) *via* a facile alcohol reduction approach.

2.4. Fabrication of Au@MIL-100(Fe) and Pt@MIL-100(Fe)

The precursors of Au and Pt ($HAuCl_4{\cdot}4H_2O$ and $H_2PtCl_6{\cdot}6H_2O$) were dissolved in deionized water directly to produce the corresponding solution with the desirable concentration, 10 mg/mL. Then, a mixture of MIL-100(Fe) (100 mg), a certain amount of metal ions aqueous solution, PVP (0.0333 g), ethanol (3 mL) and H_2O (12 mL) was added into a 50 mL round bottom flask. And the rest of the procedure of the above suspension was the same as that of Pd@MIL-100(Fe).

2.5. Characterizations

XRD patterns were carried on a Bruker D8 Advance X-ray diffrractometer operated at 40 kV and 40 mA with Ni-filtered Cu Ka irradiation ($\lambda = 0.15406$ nm). The data were recorded in the 2θ range of 3–40°. Scanning electron microscopy (SEM) images were obtained on a Hitachi SU8000 scanning microscope at an accelerating voltage of 10 kV. UV–vis diffuse reflectance spectra (DRS) were recorded on a Cary-500 UV–vis-NIR spectrometer in which $BaSO_4$ powder was used as the internal standard. Nitrogen adsorption–desorption isotherms and the Brunauer–Emmett–Teller (BET) surface areas were collected at 77 K using Micromeritics ASAP2010 equipment. Transmission electron microscopy (TEM) and high-resolution transmission electron microscopy (HRTEM) images were measured using a JEOL model JEM2010 EX microscope at an accelerating voltage of 200 kV. X-ray photoelectron spectroscopy (XPS) measurements were conducted on a PHI Quantum 2000 XPS system equipped with an Al X-ray source (1486.6 eV). The Brunauer–Emmett–Teller (BET) surface area was measured with an ASAP2020 M apparatus (Micromeritics Instrument Corp., USA). The concentration of Fe(III) in the supernate was detected by the Ultima2 ICP optical emission spectrometer. The mineralization degree of dyes aqueous solutions was detected by total organic carbon (TOC) value, which obtained by a Shimadzu TOC-VCPH analyzer. The Mott–Schottky analysis and the electrochemical impedance spectroscopy (EIS) were performed at a Zahner electrochemical workstation. The photocurrent measurements were conducted on a Precision PARC workstation. The photoluminescence (PL) spectrum for samples were conducted on an Edinburgh FL/FS900 spectrophotometer. Cyclic voltammograms (CVs) were recorded by a CHI 810B electrochemical workstation. The measurement was performed in a conventional three-electrode cell, with a glassy carbon electrode as the working electrode, Pt plate and Ag/AgCl electrode as the counter electrode and reference electrode, respectively.

2.6. Evaluation of photocatalytic activity

The photocatalytic performance of the as-prepared samples was evaluated by the degradation of PPCPs under visible light irradia-

tion. In the photoactivity text, 5 mg of photocatalyst was suspended in 40 mL of PPCPs aqueous solution (20 mg/L), and the pH value of reaction solution (pH 4) was adjusted with 2 mol/L H_2SO_4 aqueous solution. After adding 40 μL of H_2O_2, the suspension was stirred for 2 h to reach adsorption–desorption equilibrium. Then the above suspension was irradiated by a 300 W Xe lamp (PLS-SXE 300, Trusttech Co., Ltd., Beijing) with 420 nm cut-off filter (420 nm ≤ λ ≤ 760 nm). As the reaction proceeded, 4 mL of suspension was taken from the reactor at a scheduled interval and centrifuged. The high performance liquid chromatography (HPLC, Agilent 1260) was employed to determine the PPCPs concentrations in the solution. Separation was carried out at about 25 °C on the Xtimate™ C18 column (4.6 mm × 150 mm, 5.0 μm particle size). The mobile phase used for the analysis of theophylline consisted of H_2O–methanol solution (35:65, v/v), at a flow rate of 0.8 mL/min, the wavelength for detection was adjusted to 272 nm. As for ibuprofen, the mobile phase consisted of H_2O–acetonitrile solution (70:30, v/v), at a flow rate of 1.3 mL/min, the wavelength for detection was adjusted to 222 nm. Moreover, the mobile phase used for the analysis of bisphenol A consisted of H_2O–methanol solution (30:70, v/v), at a flow rate of 0.7 mL/min, the wavelength for detection was adjusted to 224 nm.

3. Results and discussion

3.1. Characterizations

Fig. 1 shows the XRD patterns of the as-prepared samples. It is obvious that the as-prepared MIL-100(Fe) and Pd@MIL-100(Fe) possess similar XRD patterns [33], implying that the crystal structure of the MIL-100(Fe) is maintained after the alcohol reduction process. However, for the Pd@MIL-100(Fe), no distinct diffraction peaks of metallic Pd are observed. This can be ascribed to the low amount of Pd in the Pd@MIL-100(Fe) nanocomposite (1 wt%) [27]. Fig. S1(A) and (B) shows typical scanning electron microscopy (SEM) images of MIL-100(Fe) and Pd@MIL-100(Fe), respectively. Clearly, the integrity of characteristic structure of MIL-100(Fe) is retained and not influenced by the reflux process. A representative transmission electron microscopy (TEM) image of MIL-100(Fe) decorated with Pd NPs is displayed in Fig. 2(A). A high dispersion of Pd NPs with the particle sizes of range from 6–10 nm can be observed (see Fig. S2). The selected area electron diffraction (SAED) pattern of Pd@MIL-100(Fe) is shown in Fig. 2(B), and the bright rings with occasional bright spots signify the crystalline nature of the Pd NPs. High-resolution TEM (HRTEM) image in Fig. 2(C) and (D) unambiguously displays that the Pd NPs disperse on the surface of the MIL-100(Fe) display the well-defined lattice fringes. The average lattice fringes of d = 0.221 nm can be indexed as the (1 1 1) plane of Pd NPs. The excellent dispersion of Pd NPs on the MIL-100(Fe) should be due to the fact that the ultrahigh surface area and the porosity of MIL-100(Fe), which can be expected on such highly dispersed Pd NPs. Moreover, the protection of PVP around Pd NPs is robust enough so that the self-aggregation of

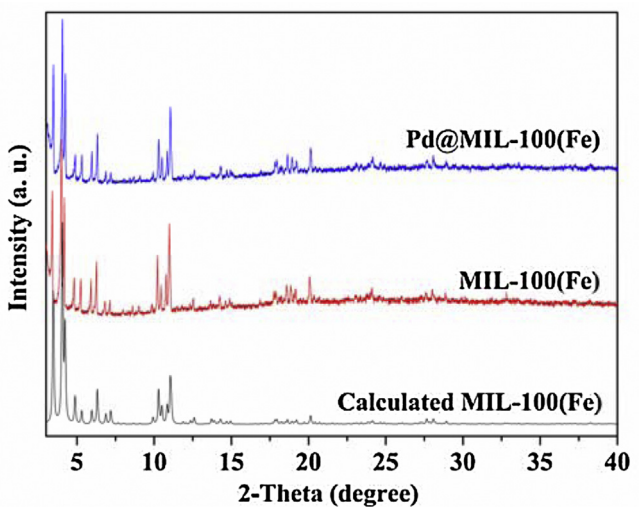

Fig. 1. XRD patterns of samples.

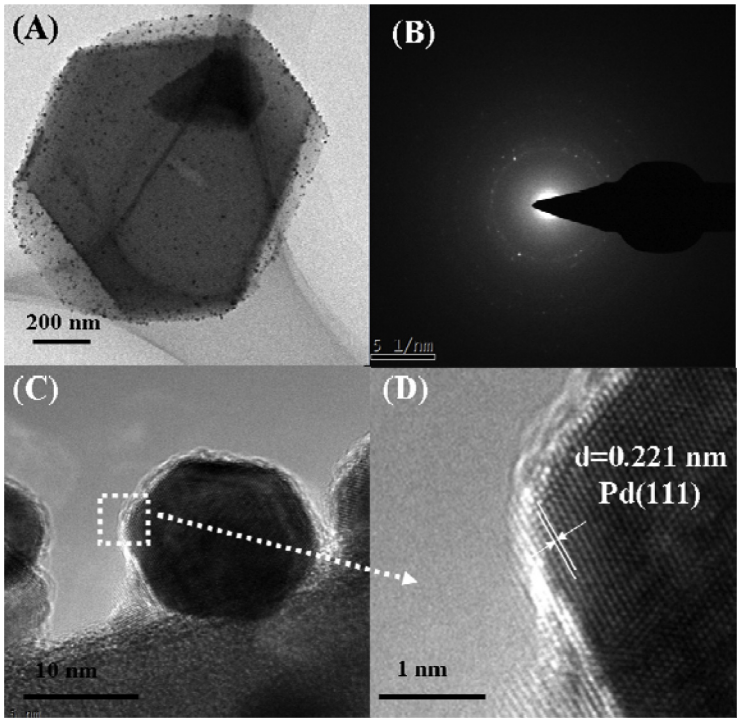

Fig. 2. (A) TEM image, (B) SAED pattern, (C and D) HRTEM image of the as-prepared Pd@MIL-100(Fe).

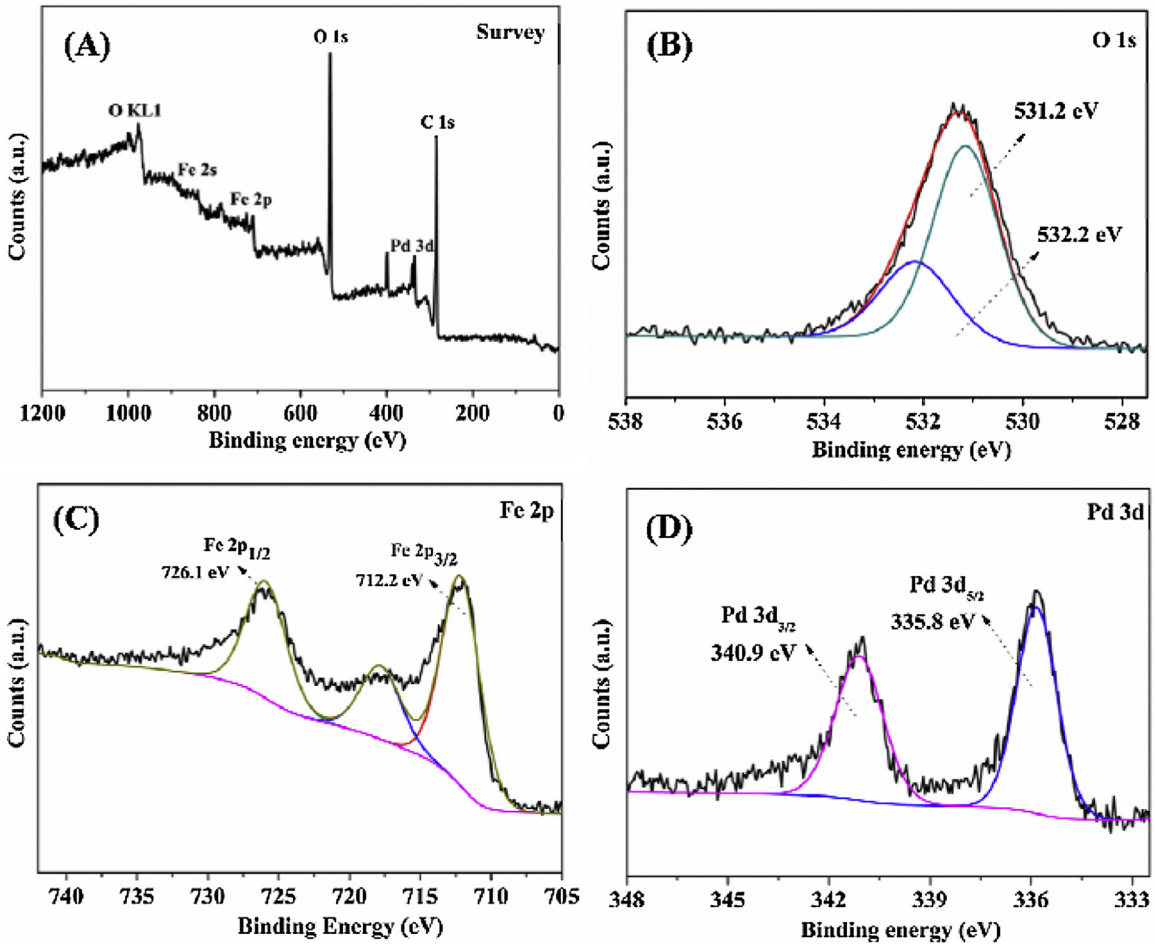

Fig. 3. XPS patterns of Pd@MIL-100(Fe).

Pd NPs is inhibited significantly during the synthesis. The results indicate that the facile alcohol reduction pathway is very useful for dispersion of Pd NPs anchored on MOFs. To confirm the elemental composition of the Pd@MIL-100(Fe), the energy-dispersive X-ray spectroscopy (EDX) has also been carried out. The result reveals that the Pd@MIL-100(Fe) contain the elements of Fe, O, C and Pd (see Fig. S3), and the weight ratio of Pd NPs in the Pd@MIL-100(Fe) nanocomposite is 0.867 wt%. It is demonstrated that the facile alcohol reduction approach is an effective technique of immobilizing Pd NPs onto the MIL-100(Fe), because the content of Pd only slightly less than the theoretical content (1 wt%).

The surface chemical states of the Pd@MIL-100(Fe) have been analyzed by X-ray photoelectron spectroscopy (XPS) measurements. The survey spectrum (see Fig. 3(A)) shows the existence of Fe, O, C and Pd in the Pd@MIL-100(Fe). The weak signal of Pd is due to the relatively low content of Pd in the Pd@MIL-100(Fe) nanocomposite. The high-resolution XPS spectrum of the O 1s could be fitted by two peaks at binding energies of around 532.2 and 531.2 eV (see Fig. 3(B)), which are attributed to the oxygen components in the BTC linkers and the Fe—O bonds, respectively [34,35]. Observation of the Fe 2p spectrum (see Fig. 3(C)), the binding energies of 712.1 and 726.0 eV are characteristic of Fe(III) in MIL-100(Fe) [23]. The peak separation, namely, $\Delta = 2p_{1/2} - 2p_{3/2} = 14.1$ eV, which is very similar to those reported for α-Fe_2O_3 [36]. As shown in Fig. 3(D), the two peaks of Pd ($3d_{5/2}$ and $3d_{3/2}$) are locate at 335.8 and 340.9 eV, respectively, which can be assigned to metallic Pd^0 [27]. This indicates that the Pd NPs are successfully immobilized on the surface of the MIL-100(Fe). Thus, the results of XRD, TEM and XPS verify the Pd@MIL-100(Fe) nanocomposite has been successfully prepared *via* a alcohol reduction approach.

In addition, the BET surface area and pore structure of the prepared samples have been investigated (see Fig. S4). It can be seen that the BET surface area of Pd@MIL-100(Fe) is 2102 m^2/g. For comparison, the corresponding BET surface area of original-MIL-100(Fe) has also been investigated (2006 m^2/g). Notice that the surface areas of the Pd@MIL-100(Fe) is increased as compared to the original-MIL-100(Fe). This could be due to the fact that the guest molecules in the pores of MIL-100(Fe) have been further removed during the reflow process (see Table S1). Thus, we can envision that a greater specific surface area of Pd@MIL-100(Fe) is expected to provide more catalytic site, leading to a superior photocatalytic performance. Fig. 4 displays the UV–vis diffuse reflectance (UV–vis DRS) spectra of as-prepared samples. Both absorption spectra of MIL-100(Fe) and Pd@MIL-100(Fe) exhibit the strong absorption bands at about 320 nm, which are assigned to the ligand-to-metal charge transfer (LMCT), implying the bonding of carboxylate oxygen to metal [37]. In addition, a small peak centered at 445 nm appears in MIL-100(Fe) and Pd@MIL-100(Fe), respectively, which may be due to the transition ($^6A_{1g} => {}^4A_{1g} + {}^4Eg(G)$) in Fe(III) [38,39]. In generally, the typical surface plasmon resonance (SPR) peak of Pd NPs is located around 300 nm [40,41]. Therefore, for Pd@MIL-100(Fe), the SPR peak of Pd could be shielded by the strong absorption of MIL-100(Fe) in the UV region. Obviously, the Pd@MIL-100(Fe) possesses much better visible light absorption intensity than MIL-100(Fe), which conforms with the color changing from saffron yellow to brown (inset in Fig. 4). Therefore, the enhanced absorbance of light is expected to improve the photoac-

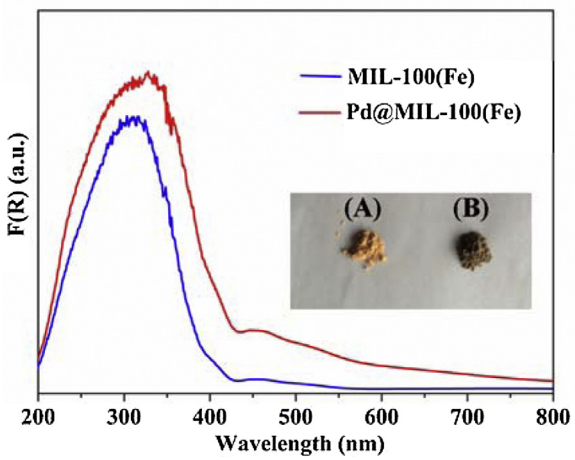

Fig. 4. UV–vis DRS spectra of MIL-100(Fe) and Pd@ MIL-100(Fe), the inset are the photographs of (A) MIL-100(Fe) and (B) Pd@ MIL-100(Fe).

tivity for a target reaction. This inference can be verified by the photocatalytic degradation of PPCPs under visible light irradiation.

3.2. Photocatalytic properties

The photocatalytic activity of the Pd@MIL-100(Fe) have been firstly evaluated by the degradation of theophylline under visible light irradiation ($\lambda \geq 420$ nm). Fig. 5(A) displays the photocatalytic degradation of theophylline under different experimental conditions. Apparently, a negligible degradation of theophylline is observed in the darkness (curve a). The degradation efficiency of theophylline is slightly enhanced when a small amount of H_2O_2 is added (no catalyst, curve b), due to the possible photolysis of H_2O_2 induced by incident light. Under visible light irradiation, Pd@MIL-100(Fe) is able to degrade about 7.3% of theophylline after 150 min (without H_2O_2, curve c), which may attribute to a direct holes oxidation pathway. Notably, Pd@MIL-100(Fe) becomes highly active by addition of a certain amount of H_2O_2 (curve d). Moreover, after visible light illumination for 150 min, the Pd@MIL-100(Fe) exhibits much higher activity than that of MIL-100(Fe) (99.5%, curve e). Importantly, Pd@MIL-100(Fe) also performs better than Pd@$TiO_{2-x}N_x$ (curve f) and Pd@Fe_2O_3 (curve g) under identical experimental conditions, respectively. To further confirm the Pd@MIL-100(Fe) with superior photocatalytic activity toward degradation of PPCPs, we have also performed the activity testing on photocatalytic degradations of ibuprofen and bisphenol A (see Fig. 5(B) and (C)). Apparently, the Pd@MIL-100(Fe) exhibits higher photoactivity than that of original-MIL-100(Fe). To determine the mineralization extent of PPCPs, the total organic carbon (TOC) values of the organic pollutants aqueous solutions have also been detected. Obviously, with the increase of irradiation time the TOC values are decreased significantly (see Table 1), which are consistent with the results of photocatalytic activity experiments.

To understand the photoactivities of M@MIL-100(Fe) (M = Au, Pd and Pt), a series of M@MIL-100(Fe) (1 wt%) have been fabricated *via* the alcohol reduction approach and applied to photocatalytic degradation of PPCPs. Obviously, different kinds of noble-metal deposition result in remarkably different photocatalytic activi-

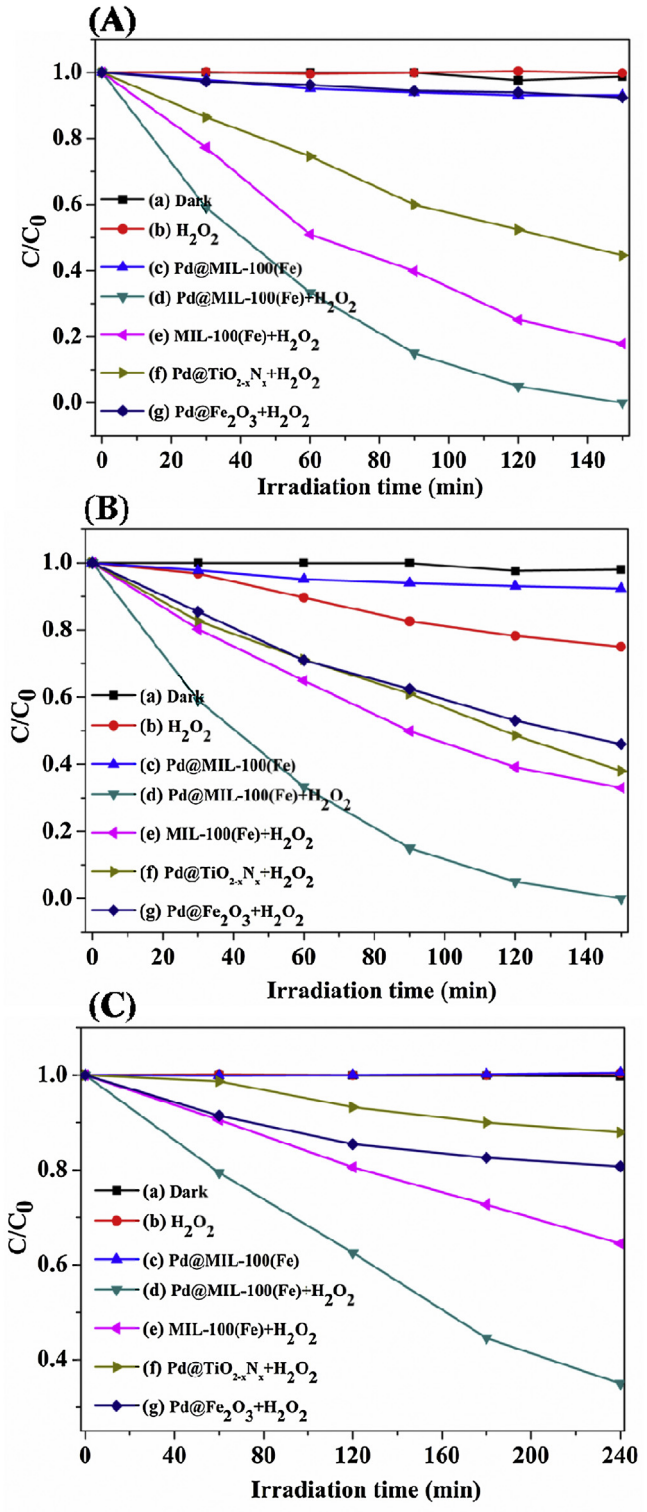

Fig. 5. Photocatalytic degradation of (A) theophylline, (B) ibuprofen and (C) bisphenol A under different conditions. Reaction conditions: 5 mg of photocatalyst, 40 mL of 20 mg/L PPCPs, 40 μL of H_2O_2, pH 4.

Table 1
Removal rate of TOC under various experiment conditions. Reaction conditions: 5 mg of photocatalyst, 40 mL of 20 mg/L PPCPs, 40 μL of H_2O_2, pH 4.

Samples	Pd@MIL-100(Fe)	MIL-100(Fe)	Pd@$TiO_{2-x}N_x$	Pd@Fe_2O_3	Pollutants
TOC removal (%)	45.2	29.4	4.2	3	Theophylline
	69.2	45.5	29.3	29	Ibuprofen
	20.5	15.6	6	11.3	Bisphenol A

ties of M@MIL-100(Fe) (see Fig. S5). Among all of the samples, the Pd@MIL-100(Fe) exhibits the highest photocatalytic activity toward the degradation efficiency of PPCPs (see Fig. S6). As shown in Fig. S7 and S8, it is crucial to control the loading amount of Pd NPs to achieve an optimal synergy interaction between Pd NPs and MIL-100(Fe) for degradation of PPCPs. When the Pd NPs content is 1 wt%, the sample shows the best photocatalytic activity. However, further increasing the loading amount of Pd NPs, the degradation ratio of PPCPs in aqueous solutions would keep unchanged. Based on the experimental results, it can conclude that 1% Pd@MIL-100(Fe) exhibits great superiority photocatalytic performance toward photocatalytic degradation of PPCPs. Thus, it is chosen as the testing candidate to investigate the effect of operating parameters on the degradation of PPCPs.

As widely accepted, the solution pH is an important factor affecting the homogeneous photocatalytic reaction [42,43]. The effect of initial pH on the degradation efficiency of PPCPs over Pd@MIL-100(Fe) has been investigated. As for the Pd@MIL-100(Fe)/theophylline system (see Fig. 6(A)), the adsorptivity of theophylline is found to strongly depend on the initial pH value, which enhanced rapidly by decreasing the pH value. Then after 120 min of visible light illumination, the degradation efficiency of theophylline over Pd@MIL-100(Fe) will also increase with the decreasing of the pH value, the degradation efficiency of theophylline is about 65%, 95% and 100% at pH 6, 4 and 2, respectively. However, for Pd@MIL-100(Fe)/ibuprofen system, an opposite tendency is observed (see Fig. 6(B)). That is, the increasing pH value would lead to a better adsorptivity of ibuprofen, which in turn leads to the enhancement of the contact between Pd@MIL-100(Fe) and ibuprofen. As a result, the degradation efficiency will increase rapidly by the increasing pH value. Moreover, we have also tested the photoactivity of Pd@MIL-100(Fe) toward degradation bisphenol A under identical experimental conditions, and a very similar phenomenon is observed (see Fig. 6(C)), *i.e.* the degradation efficiency is enhanced significantly by the increasing initial pH value.

Furthermore, the influence of H_2O_2 dosage on the degradation of PPCPs over Pd@MIL-100(Fe) has also been evaluated and the results are shown in Fig. S9. With the absence of H_2O_2 the degradation efficiency is very slow, after 150 min of continuous reaction the degradation efficiency of theophylline is below 10%; when 20 μL of H_2O_2 is added, the degradation efficiency is rapidly increased to 77%. Moreover, when the amount of H_2O_2 is increased to 40 μL, the highest photocatalytic activity is obtained. After 150 min of visible light illumination, almost 100% theophylline can be degraded. Nevertheless, when further increasing of H_2O_2 amount, the degradation efficiency of theophylline in aqueous solutions would keep unchanged. It can be explained that surplus H_2O_2 could perform as a scavenger of $^{\bullet}OH$ to generate hydroperoxyl radicals ($^{\bullet}HOO$) with lower oxidation potential (Eqs. (1) and (2)) [44,45]. We have also performed the activity testing on photocatalytic degradation ibuprofen and bisphenol A over Pd@MIL-100(Fe) with different amount of H_2O_2 under visible light irradiation, for which similar activity trend is also observed (see Fig. S9).

$$H_2O_2 + {}^{\bullet}OH \rightarrow H_2O + {}^{\bullet}HOO \quad (1)$$

$$^{\bullet}HOO + {}^{\bullet}OH \rightarrow H_2O + O_2 \quad (2)$$

3.3. Reusability and stability of Pd@MIL-100(Fe)

The stability and reusability of Pd@MIL-100(Fe) have also been investigated. In our work, the photocatalyst was recovered by filtration, washed with ethanol and water to completely remove the absorbed PPCPs on the surface of catalyst. And then, the photocatalyst was collected and blow-dried with N_2. As shown in Fig. 7, photocatalytic activity of Pd@MIL-100(Fe) does not obviously decrease after four cycles, suggesting that the Pd@MIL-100(Fe) photocatalyst possesses high stability in these reaction systems. Moreover, the XRD patterns (see Fig. S10(A)) and XPS patterns (see Fig. S10(B)) of Pd@MIL-100(Fe) before and after the reaction reveal that the crystal structure and surface chemical compositions of Pd@MIL-100(Fe) still keep unchanged even after the

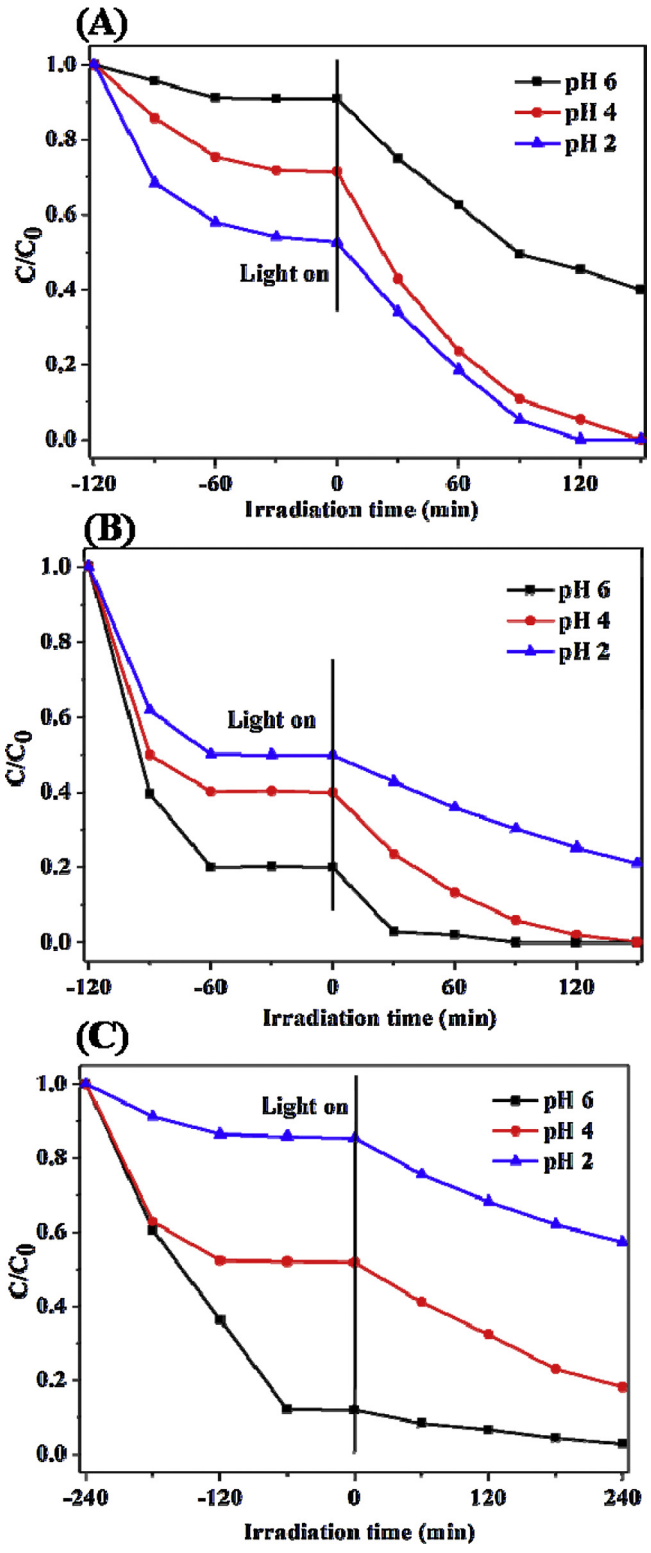

Fig. 6. Effect of initial pH value on the degradation of (A) theophylline, (B) ibuprofen and (C) bisphenol A over Pd@MIL-100(Fe) under visible light irradiation. Reaction conditions: 5 mg of Pd@MIL-100(Fe), 40 mL of 20 mg/L PPCPs, 40 μL of H_2O_2.

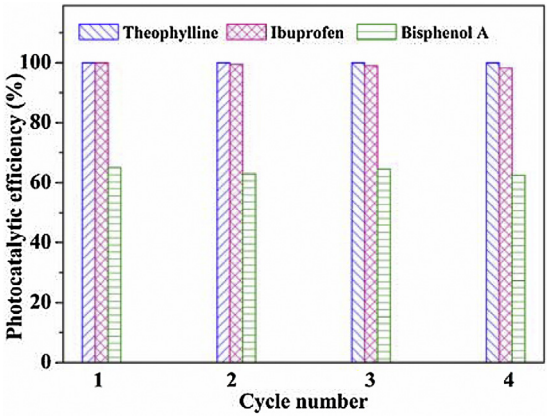

Fig. 7. Reusability of Pd@MIL-100(Fe) for the photocatalytic degradation of PPCPs. Reaction conditions: 5 mg of Pd@MIL-100(Fe), 40 mL of 20 mg/L PPCPs, 40 μL of H_2O_2, pH 4.

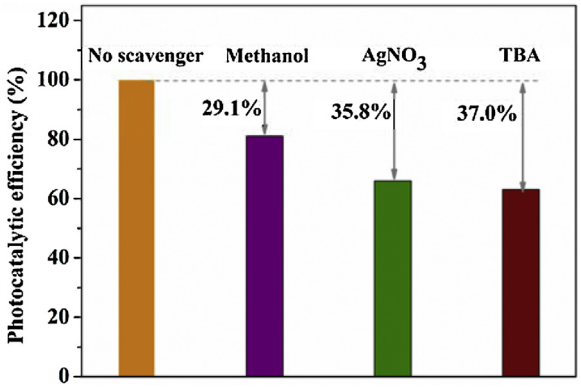

Fig. 8. The photocatalytic degradation of theophylline over Pd@MIL-100(Fe) under visible light irradiation in the presence of radical scavengers (0.1 mmol).

four cycles of the reaction. Furthermore, the amount of Fe(III) ions leaching during the reaction has been quantified by ICP optical emission spectrometer (see Table S2–S4). After the dark adsorption treatment, the ICP result shows that only a small amount of Fe(III) leaching from photocatalyst. Considering the fact that the MOFs materials are very sensitive to the solvent, the result is reasonable. To further study the stability of Pd@MIL-100(Fe) during the photocatalytic process, the concentration of Fe(III) ions leaching during the reaction has also been collected. Clearly, with the increase of irradiation time, there is almost no Fe(III) ions leaching from the Pd@MIL-100(Fe). Additionally, cyclic voltammetry measurement (CV) has also been performed to verify the photochemical stability of Pd@MIL-100(Fe). Taking Pd@MIL-100(Fe)/theophylline/H_2O_2 system as an example, as shown in Fig. S11, no obvious responses are observed in the absence of additives (curve a). Then, Pd@MIL-100(Fe) suspension is decorated onto a glassy carbon electrode (GCE) and dried in air as working electrode (denote as MOF/GCE). For MOF/GCE, a remarkable oxidation peak at about 1.5 V is observed (curve b). However, after injecting 2 μL of theophylline into this system, the oxidation peak displays a slight shift toward the negative potential, and the peak current decrease significantly (curve c). After further injecting 2 μL of H_2O_2, a very similar phenomenon is observed (curve d). Evidently, the more negative oxidation potential and the large decreased peak current clearly demonstrate that the addition of certain amount of theophylline and H_2O_2 could restrain the self-decomposition of catalyst effectively. Combining the above results, it can be concluded that

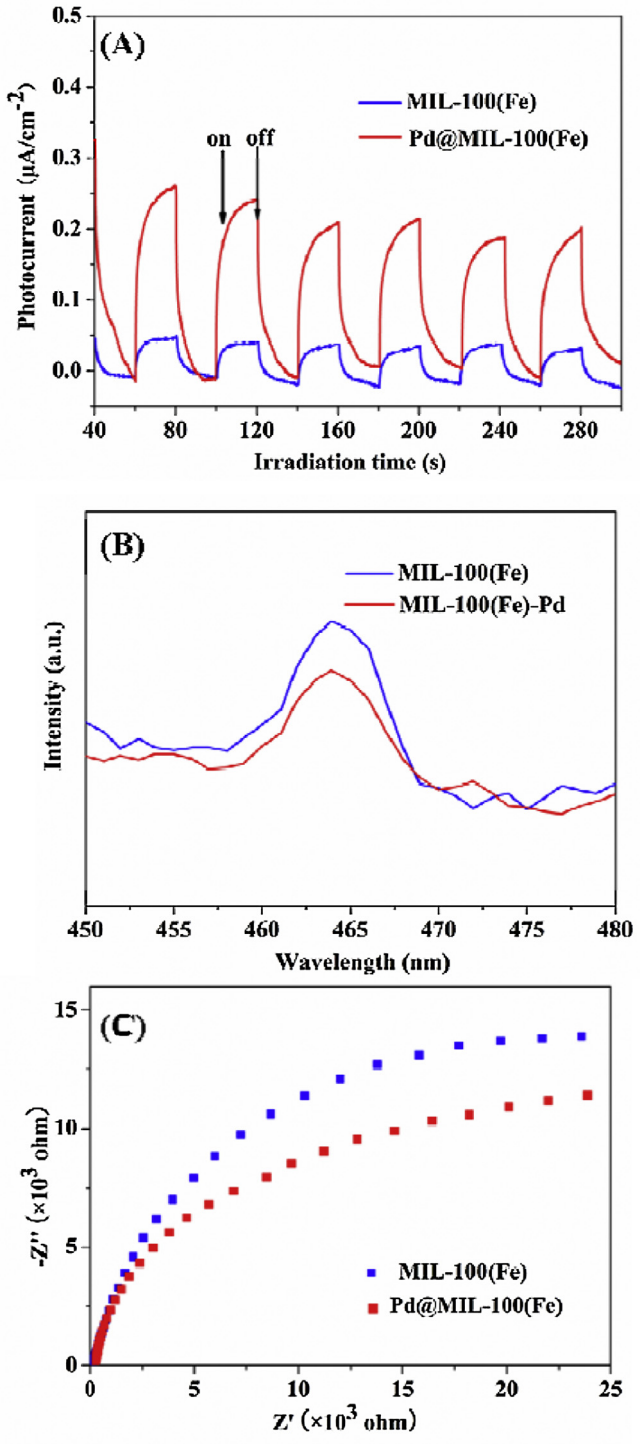

Fig. 9. (A) Transient photocurrent response, (B) photoluminescence (PL) spectra and (C) Nyquist impedance plots of MIL-100(Fe) and Pd@MIL-100(Fe).

the Pd@MIL-100(Fe) photocatalyst possesses high stability and reusability.

3.4. Mechanism for the PPCPs degradation over Pd@MIL-100(Fe)

To gain more insight into the reaction, a series of active species trapping experiments with different radical scavengers have been performed. Taking Pd@MIL-100(Fe)/theophylline system as an example, as displayed in Fig. 8. About 29.1%, 35.8% and 37.0% suppression are observed when methanol (a hole scavenger),

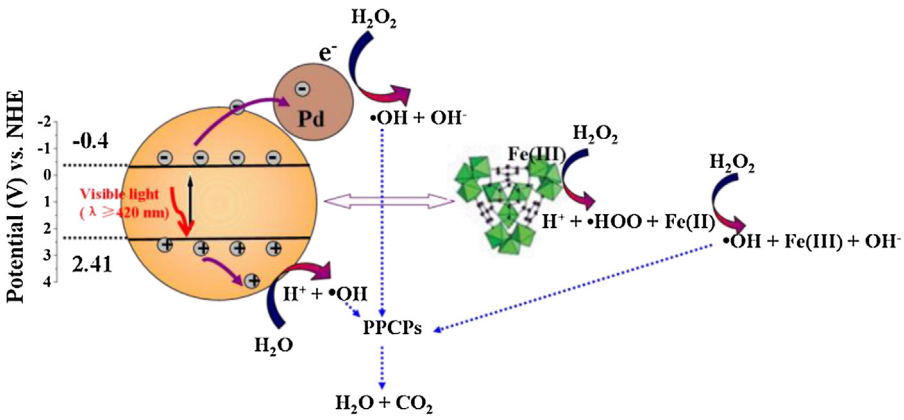

Fig. 10. Proposed mechanism for the photocatalytic degradation of PPCPs over Pd@MIL-100(Fe) under visible light irradiation.

$AgNO_3$ (an electron scavenger) and *tert*-butyl alcohol (TBA, a •OH scavenger) are added to photocatalytic reaction systems, respectively. The obvious inhibitory effect of $AgNO_3$ and TBA manifests that the photogenerated electron and •OH play major roles for photocatalytic degradation of PPCPs. Moreover, electrochemical analyses have been used to investigate the effect of the Pd NPs in the Pd@MIL-100(Fe). Fig. 9(A) displays the photocurrent–time (I–t) curves of as-prepared products under intermittent visible light illumination. It is obvious that Pd@MIL-100(Fe) exhibits a higher photocurrent density than that of MIL-100(Fe), suggesting a more efficient separation of the photoexcited electron–hole pairs of Pd@MIL-100(Fe). This can be further confirmed by the photoluminescence (PL) spectra. Fig. 9(B) shows the PL spectra of MIL-100(Fe) and Pd@MIL-100(Fe), which are obtained at room temperature with an excitation wavelength of 340 nm. Apparently, the introduction of Pd NPs could lower the PL intensity, suggesting the longer lifetime of photogenerated charge carriers in Pd@MIL-100(Fe) than those of MIL-100(Fe). To investigate the photogenerated charge separation efficiency of these two samples, the electrochemical impedence spectroscopy (EIS) has been carried out. As displayed in Fig. 9(C), Pd@MIL-100(Fe) has the smaller arc as compared to the original-MIL-100(Fe), meaning that Pd NPs can facilitate the interfacial charge transfer.

In addition, Mott–Sckottky measurements have been also performed in darkness. As shown in Fig. S12, the flat-band potential of Pd@MIL-100(Fe) determined from Mott–Schottky plots is *ca.* −0.60 V *vs.* Ag/AgCl at pH 6.8, corresponding to a potential of −0.40 V *vs.* NHE at pH 6.8 [46,47]. Combined with the band gap energy estimated from UV–vis DRS spectrum, valence band (VB) of Pd@MIL-100(Fe) is calculated to be 2.41 V *vs.* NHE, which is more positive than the •OH/H_2O potential (1.23 V *vs.* NHE). It is thermodynamically permissible for the H_2O is trapped by photogenerated holes to form •OH possesses a strong oxidation capacity and can also oxidize the surface adsorbed organic molecules (Eqs. (3) and (4)). On the one hand, the H_2O_2 serves as an efficient scavenger that could capture the photogenerated electrons to form more •OH radicals (Eq. (5)), thus further enhancing photocatalytic activity. On the other hand, the Fe(III)–O clusters on the surface of Pd@MIL-100(Fe) can catalyze the decomposition of H_2O_2 to produce •OH radicals by the Fenton-like reaction (Eqs. (6) and (7)). Accordingly, the above processes could cooperatively contribute to the activation of H_2O_2 by Pd@MIL-100(Fe) to produce more •OH radicals, thus greatly enhancing the degradation efficiency of PPCPs (see Fig. 10).

$$h\nu \geq E_{bg}$$

$$\text{Pd@MIL-100(Fe)} \rightarrow \text{Pd@MIL-100(Fe)}(h^+ + e^-) \quad (3)$$

$$h^+ + H_2O \rightarrow {}^\bullet OH + H^+ \quad (4)$$

$$e^- + H_2O_2 \rightarrow {}^\bullet OH + OH^- \quad (5)$$

$$\text{Fe(III)species} + H_2O_2 \rightarrow \text{Fe(II)species} + {}^\bullet HOO + H^+ \quad (6)$$

$$\text{Fe(II)species} + H_2O_2 \rightarrow \text{Fe(III)species} + {}^\bullet OH + OH^- \quad (7)$$

4. Conclusions

In summary, highly dispersed Pd@MIL-100(Fe) nanocomposite has been successfully prepared *via* a facile alcohol reduction method. The resulting Pd@MIL-100(Fe) exhibits improved activity compared with the MIL-100(Fe) toward the photocatalytic degradation of PPCPs under visible-light illumination ($\lambda \geq 420$ nm). The higher photoactivity of Pd@MIL-100(Fe) can be ascribed to the synergistic effect of the enhanced light absorption intensity and more efficient separation of the charge-carrier as well as the increased surface area. The visible light photocatalytic activities of the samples are found to be closely dependent on the deposition of different noble-metals and the loading amount of Pd. Experimental results reveal that the 1% Pd@MIL-100(Fe) exhibits great superiority photocatalytic performance toward photocatalytic degradation of PPCPs. Moreover, the addition of H_2O_2 and pH value of the reaction solution also played important roles in the photocatalytic processes. Herein, we show for the first time that a novel Pd@MOFs nanocomposite can be fabricated *via* a facile alcohol reduction approach and applied to the photocatalytic treatment of PPCPs. It is hoped that this work could offer a simple strategy on fabricating of such MOF-based nanocomposites as visible light photocatalysts for environmental restoration.

Acknowledgements

This work was supported by the National Natural Science Foundation of China (21273036 and 21177024) and Science & Technology Plan Project of Fujian Province (2014Y2003)

Appendix A. Supplementary data

Supplementary data associated with this article can be found, in the online version, at http://dx.doi.org/10.1016/j.apcatb.2015.04.009.

References

[1] C. Ort, M.G. Lawrence, J. Rieckermann, A. Joss, Environ. Sci. Technol. 44 (2010) 6024–6035.
[2] C. Martínez, L.M. Canle, M.I. Fernández, J.A. Santaballa, J. Faria, Environ. Appl. Catal. B 102 (2011) 563–571.

[3] S.A. Snyder, P. Westerhoff, Y. Yoon, D.L. Sedlak, Environ. Eng. Sci. 20 (2003) 449–469.
[4] A. Joss, H. Andersen, T. Ternes, P.R. Richle, H. Siegrist, Environ. Sci. Technol. 38 (2004) 3047–3055.
[5] S.A. Snyder, E.C. Wert, D.J. Rexing, R.E. Zegers, D.D. Drury, Ozone: Sci. Eng. 28 (2006) 445–460.
[6] P. Westerhoff, Y. Yoon, S. Snyder, E. Wert, Environ. Sci. Technol. 39 (2005) 6649–6663.
[7] A. Hu, X. Zhang, D. Luong, K.D. Oakes, M.R. Servos, R. Liang, S. Kurdi, P. Peng, Y. Zhou, Waste Biomass Valor. 3 (2012) 443–449.
[8] J. Bai, Y. Liu, J. Li, B. Zhou, Q. Zheng, W. Cai, Appl. Catal. B: Environ. 98 (2010) 154–160.
[9] P. Calza, V.A. Sakkas, A. Villioti, C. Massolino, V. Boti, E. Pelizzetti, T. Albanis, Appl. Catal. B: Environ. 84 (2008) 379–388.
[10] C. Martínez, S. Vilariño, M.I. Fernández, J. Faria, L.M. Canle, J.A. Santaballa, Environ. Appl. Catal. B 142–143 (2013) 633–646.
[11] P.M. Álvarez, J. Jaramillo, F. López-Piñero, P.K. Plucinski, Appl. Catal. B: Environ. 100 (2010) 338–345.
[12] J. Xu, L. Li, C. Guo, Y. Zhang, W. Meng, Appl. Catal. B: Environ. 130–131 (2013) 285–292.
[13] G. Ferey, Chem. Soc. Rev. 37 (2008) 191–214.
[14] A.R. Millward, O.M. Yaghi, J. Am. Chem. Soc. 127 (2005) 17998–17999.
[15] B.V. Harbuzaru, A. Corma, F. Rey, P. Atienzar, J.L. Jordá, H. García, D. Ananias, L.D. Carlos, J. Rocha, Angew. Chem. Int. Ed. 47 (2008) 1080–1083.
[16] M. Vallet-Regi, F. Balas, D. Arcos, Angew. Chem. Int. Ed. 46 (2007) 7548–7558.
[17] C. Janiak, Dalton Trans. (2003) 2781–2804.
[18] D. Farrusseng, S. Aguado, C. Pinel, Angew. Chem. Int. Ed. 48 (2009) 7502–7513.
[19] R. Liang, L. Shen, F. Jing, W. Wu, N. Qin, R. Lin, L. Wu, Appl. Catal. B: Environ. 162 (2015) 245–251.
[20] L. Shen, M. Luo, Y. Liu, R. Liang, F. Jing, L. Wu, Appl. Catal. B: Environ. 166–167 (2015) 445–453.
[21] P. Mahata, G. Madras, S. Natarajan, J. Phys. Chem. B 110 (2006) 13759–13768.
[22] F.X. Llabrés i Xamena, A. Corma, H. García, J. Phys. Chem. C 111 (2006) 80–85.
[23] R. Liang, F. Jing, L. Shen, N. Qin, L. Wu, J. Hazard. Mater. 287 (2015) 364–372.
[24] L. Shen, S. Liang, W. Wu, R. Liang, L. Wu, Dalton Trans. 42 (2013) 13649–13657.
[25] M. Müller, S. Turner, O.I. Lebedev, Y. Wang, G. van Tendeloo, R.A. Fischer, Eur. J. Inorg. Chem. 12 (2011) 1876–1887.
[26] H.R. Moon, D.W. Lim, M.P. Suh, Chem. Soc. Rev. 42 (2013) 1807–1824.
[27] L. Shen, W. Wu, R. Liang, R. Lin, L. Wu, Nanoscale 5 (2013) 9374–9382.
[28] D. Esken, X. Zhang, O.I. Lebedev, F. Schroder, R.A. Fischer, J. Mater. Chem. 19 (2009) 1314–1319.
[29] M. Sabo, A. Henschel, H. Frode, E. Klemm, S. Kaskel, J. Mater. Chem. 17 (2007) 3827–3832.
[30] M.S. Al-Shall, V. Abdelsayed, A.E.R.S. Khder, H.M.A. Hassan, H.M. El-Kaderi, T.E. Reich, J. Mater. Chem. 19 (2009) 7625–7763.
[31] L.J. Murray, M. Dinca, J.R. Long, Chem. Soc. Rev. 38 (2009) 1294–1314.
[32] C.F. Zhang, L.G. Qiu, F. Ke, Y.J. Zhu, Y.P. Yuan, G.S. Xu, X. Jiang, J. Mater. Chem. A 1 (2013) 14329–14334.
[33] P. Horcajada, S. Surble, C. Serre, D.Y. Hong, Y.K. Seo, J.S. Chang, J.M. Greneche, I. Margiolaki, G. Ferey, Chem. Commun. (Camb.) (2007) 2820–2822.
[34] S.K. Das, M.K. Bhunia, M. Motin Seikh, S. Dutta, A. Bhaumik, Dalton Trans. 40 (2011) 2932–2939.
[35] S.K. Tam, J. Dusseault, S. Polizu, M. Menard, J.P. Halle, L. Yahia, Biomaterials 26 (2005) 6950–6961.
[36] C. Yu, L. Gou, X. Zhou, N. Bao, H. Gu, Electrochim. Acta 56 (2011) 9056–9063.
[37] S. Bordiga, C. Lamberti, G. Ricchiardi, L. Regli, F. Bonino, A. Damin, K.P. Lillerud, M. Bjorgen, A. Zecchina, Chem. Commun. (2004) 2300–2301.
[38] G.T. Vuong, M.H. Pham, T.O. Do, Dalton Trans. 42 (2013) 550–557.
[39] G.T. Vuong, M.H. Pham, T.O. Do, CrystEngComm 15 (2013) 9694.
[40] N. Zhang, S. Liu, X. Fu, Y.J. Xu, J. Phys. Chem. C 115 (2011) 22901–22909.
[41] N. Zhang, Y.J. Xu, Chem. Mater. 25 (2013) 1979–1988.
[42] H. Yang, G. Lia, T. Ana, Y. Gao, J. Fua, Catal. Today 153 (2010) 200–207.
[43] G. Chen, M. Sun, Q. Wei, Z. Ma, B. Du, Appl. Catal. B: Environ. 125 (2012) 282–287.
[44] L. Ai, C. Zhang, L. Li, J. Jiang, Appl. Catal. B: Environ. 148–149 (2014) 191–200.
[45] Q. Chen, P. Wu, Y. Li, N. Zhu, Z. Dang, J. Hazard. Mater. 168 (2009) 901–908.
[46] V. Spagnol, E. Sutter, C. Debiemme-Chouvy, H. Cachet, B. Baroux, Electrochim. Acta 54 (2009) 1228–1232.
[47] A. Ishikawa, T. Takata, J.N. Kondo, M. Hara, H. Kobayashi, K. Domen, J. Am. Chem. Soc. 124 (2002) 13547–13553.